

Draft June 21, 2018

FAR ULTRAVIOLET CONTINUUM EMISSION: APPLYING THIS DIAGNOSTIC TO THE CHROMOSPHERES OF SOLAR-MASS STARS

Jeffrey L. Linsky¹*JILA, University of Colorado and NIST, 440UCB Boulder, CO 80309-0440, USA*

jlinsky@jilau1.colorado.edu

Rachel Bushinsky

*APS, University of Colorado, 391UCB Boulder, CO 80309-0391, USA*Tom Ayres¹*CASA, University of Colorado, 593UCB Boulder, CO 80309-0593, USA*

Juan Fontenla

LASP, University of Colorado, 590UCB Boulder, CO 80309-0590, USA

and

Kevin France

CASA, University of Colorado, 593UCB Boulder, CO 80309-0593, USA

ABSTRACT

The far ultraviolet (FUV) continuum flux is recognized as a very sensitive diagnostic of the temperature structure of the Sun's lower chromosphere. Until now analysis of the available stellar FUV data has shown that solar-type stars must

¹Guest Observer, NASA/ESA *Hubble Space Telescope* and User of the Data Archive at the Space Telescope Science Institute. STScI is operated by the Association of Universities for Research in Astronomy, Inc., under NASA contract NAS 5-26555. These observations were made as parts of programs #11532, #11534, and #11687.

also have chromospheres, but quantitative analyses of stellar FUV continua require far higher quality spectra and comparison with new non-LTE chromosphere models. We present accurate far ultraviolet (FUV, 1150–1500 Å) continuum flux measurements for solar-mass stars, made feasible by the high throughput and very low detector background of the Cosmic Origins Spectrograph (COS) on the *Hubble Space Telescope*. We show that the continuum flux can be measured above the detector background even for the faintest star in our sample. We find a clear trend of increasing continuum brightness temperature at all FUV wavelengths with decreasing rotational period, which provides an important measure of magnetic heating rates in stellar chromospheres. Comparison with semiempirical solar flux models shows that the most rapidly rotating solar-mass stars have FUV continuum brightness temperatures similar to the brightest faculae seen on the Sun. The thermal structure of the brightest solar faculae therefore provides a first-order estimate of the thermal structure and heating rate for the most rapidly rotating solar-mass stars in our sample.

Subject headings: stars: chromospheres — stars: individual(HII314, EK Dra, π^1 UMa, χ^1 Ori, HD 25825, HD 209458, α Cen A, Sun) — ultraviolet: stars

1. INTRODUCTION

Above the solar photosphere, the conversion of magnetic and wave energies into heat produces a thermal inversion called the chromosphere. Stars with spectral types later than about A7 V have convective zones, magnetic dynamos, and chromospheres, although the heating processes may change with stellar effective temperature and magnetic field structure. The thermal structures and energy budgets of different regions of the solar chromosphere have been studied by analysis of emission lines such as the Ca II H and K lines and the far ultraviolet (FUV) continuum flux. Semiempirical solar chromosphere models, such as those computed by Vernazza et al. (1976), Vernazza et al. (1981), Avrett & Loeser (2008), and Fontenla et al. (2009) are based in large part on fitting the observed FUV continuum.

Until recently, it has not been possible to measure accurate FUV continuum fluxes of solar-type stars because of their faint signal and large instrumental background noise produced by detector dark current and scattered light. For example, Franchini et al. (1998) showed that scattered light below 1500 Å is a large portion of the signal obtained by the International Ultraviolet Explorer (IUE) satellite, although they could approximately correct the data for scattered light. Also detector background is clearly present in the far-UV as the contrast between emission lines and the flux between the emission lines is often very low.

As a result, chromosphere models of solar-type stars (e.g., Vieytes et al. 2005) are typically based on fitting only the Ca II H and K and hydrogen Balmer emission lines. However, these emission lines are formed at the base of the chromosphere, whereas in the Sun the FUV continuum flux at wavelengths shortward of 1500 Å is formed in, and is diagnostic of, the chromospheric temperature rise from the temperature minimum.

Franchini et al. (1998) showed that G-star photospheric models with a monotonic decrease in temperature with height severely underpredict the observed UV flux below 2000 Å. The addition of an extended temperature minimum structure with an empirical value of T_{\min} provides better fits to the spectral flux of G-type stars between 1600 and 2000 Å, but such models severely underpredict the flux at shorter wavelengths (Franchini et al. 1998; Morossi et al. 2003). To fit the observed FUV flux below 1600 Å requires temperatures rising with height above the temperature minimum – a chromosphere. Using a semi-empirical solar chromospheric model, Morossi et al. (2003) could approximately fit the FUV spectrum of HD 131156 (ξ Boo A).

Franchini et al. (1998) and Morossi et al. (2003) thus demonstrated that the FUV flux below 1600 Å requires that solar type stars have solar-like chromospheres. Unfortunately, the available but rather noisy IUE data could not provide accurate measurements of the far-UV continuum uncontaminated by detector background and weak emission lines and only a few higher-quality by low-resolution HST/GHRS G140L spectra were available for analysis. Their comparison of the ξ Boo A spectrum with scaled solar-models including a chromosphere temperature structure was also uncertain as the spectral fitting software assumed LTE and the bound-free opacity of neutral metals that dominates the far-UV continuum depends on non-LTE processes. As a result, they were not able to find any trends in the far-UV emission with stellar rotation rate or other indicators of stellar magnetic activity.

What has been lacking in the previous studies is the availability of accurate FUV continuum fluxes of solar-type stars with a range of magnetic activity that can be fitted with semi-empirical non-LTE models of stellar chromospheres. We show in this paper that the combination of high throughput and very low detector background of the Cosmic Origins Spectrograph (COS) on HST now permits FUV continuum measurements for many stars. We analyze here COS observations of six stars with masses close to solar, but with a wide range of rotational periods.

Solar-mass stars reach the zero-age main sequence after their pre-main sequence evolution as rapid rotators with strong magnetic fields. As they age on the main sequence, the torque of their magnetized winds slows their rotation (e.g., Matt & Pudritz 2008), producing many profound changes in their magnetic structure and emission properties. Wilson (1963) and Kraft (1967), among others, showed that the strength of the chromospheric Ca II lines

decreases with age and rotational velocity for solar-type stars. Other changes also occur in the X-ray (e.g., Pizzolato et al. 2003), UV (e.g., Simon et al. 1985), and radio emission, starspot properties, and magnetic field structure. These changes with rotation suggest that the FUV continuum should also depend on rotation rate, but this suggestion has until now not been properly tested.

2. *HST* OBSERVATIONS OF SOLAR-MASS STARS

Our sample of solar-mass stars extending over a range of rotation periods and ages (see Table 1) was observed with the G130M grating on COS as portions of three *Hubble Space Telescope* programs. For a description of the COS instrument and its on-orbit performance, see Osterman et al. (2011). The resolving power of the COS G130M grating is $R \approx 17,000$ – $18,000$. We processed the data with the COS calibration pipeline, CALCOS¹ v2.11, combined with a custom IDL coaddition procedure. Table 1 provides details of these observations, and Figure 1 shows portions of these spectra.

The fastest rotating star in our sample is the Pleiades Cluster star HII314 (G1 V) with a rotation period $P_{\text{rot}} = 1.27$ days (Rice & Strassmeier 2001). We observed this star for 4611 seconds in program 11532 covering the spectral range $1134 \leq \lambda \leq 1459$ with four central wavelength settings ($\lambda 1291$, $\lambda 1300$, $\lambda 1309$, and $\lambda 1318$) to minimize fixed-pattern noise in the detector.

HD 209458 is the G0 V host star of the extensively studied exoplanet HD 209458b. The rotational period $P_{\text{rot}} = 11.4$ days was measured by Silva-Valio (2008) from occultations of starspots by its transiting planet. We observed HD 209458 for a total of 25641 seconds in program 11534 during transit, secondary eclipse, and both quadratures, as described by France et al. (2010a) and Linsky et al. (2010). We analyze here the combined data outside of transit from the same four central wavelength settings used for HII314 including the wavelength range 1140–1450 Å. We also include the G160M observations described by France et al. (2010a) to extend the wavelength range to 1500 Å.

EK Dra (G1 V), π^1 UMa (G1.5 V), χ^1 Ori (G1 V), and HD 25825 (G0 V) were observed as part of SNAP program 11687 with partial orbit observations at the $\lambda 1291$ central wavelength setting and two FP-POS positions (3&4) to mitigate fixed patterns. These observations cover the wavelength region 1290–1430 Å. The results of this SNAP program, with

¹We refer the reader to the cycle 18 COS Instrument Handbook for more details: http://www.stsci.edu/hst/cos/documents/handbooks/current/cos_cover.html

the objective to study the Fe XXI 1354 Å coronal emission line, will be presented elsewhere, although Ayres & France (2010) have discussed the EK Dra emission line data. Exposure times for the four stars in the SNAP program selected for this study were between 1160 and 1300 seconds. These data were reduced in the same way as described for HII314. EK Dra is a member of the Pleiades Moving Group, π^1 UMa and χ^1 Ori are members of the Ursa Major Moving Group, and HD 25825 is a member of the Hyades Cluster. Rotational velocities for these stars are listed in Table 1. The ages listed in Table 1 are from Ribas et al. (2005) and Barnes (2007).

We include for comparison the very high-resolution ($R = 114,000$) STIS E140H spectrum of α Cen A (G2 V) (Pagano et al. 2004), a slowly rotating near twin of the Sun. The data were taken from the StarCAT STIS spectral catalog (Ayres 2010). Although the detector noise background of the FUV channel of STIS is much larger than for COS, the strong signal of this nearby star makes FUV continuum measurements feasible.

2.1. Comparison Solar Irradiance Measurements

We also compare the FUV continuum fluxes of the solar-mass stars with corresponding solar irradiance measurements, which are flux values of the Sun viewed as an unresolved source. We use the solar irradiance reference spectrum obtained with the Solar Radiation and Climate Experiment (SORCE) on the Solar-Stellar Irradiance Comparison Experiment II (SOLSTICE II) (Woods et al. 2009; McClintock et al. 2005; Snow et al. 2005). These data cover the 1150–3200 Å spectral range with 1 Å resolution. We selected these data because the absolute flux calibration is accurate to about 5% in the FUV and is cross-checked against B and A-type stars. Scattered and stray light were removed from this data set. We use here the 2008 April 10–16 irradiances that represent the Sun very close to minimum with a Zurich sunspot number of 2 and an average 10.7 cm radio flux of $68.9 \times 10^{-22} \text{ Wm}^{-2}\text{Hz}^{-1}$.

2.2. Measurement of the COS Instrumental Background

There are three sources of background that must be evaluated before we can reliably ascribe the measured fluxes to stellar FUV continuum emission. First, the Exposure Time Calculator² (ETC) for the COS instrument estimates that the accumulated FUV sky background is below 10^{-3} counts over the duration of each COS observation and can therefore

²<http://etc.stsci.edu/etc/input/cos/spectroscopic/>

be ignored. Second, prior to launch, Osterman et al. (2002) measured the amount of light scattered into a 1 Å bandpass by the G130M grating to be less than $< 2 \times 10^{-5}$ of all light within ± 10 Å. This very low value rules out any significant contribution to the background, except perhaps within 10 Å of the Lyman- α line center. The on-orbit scattered-light level has been estimated to be twice as large, but this will also not be significant. Finally, detector noise is the most important background. The on-orbit-measured detector count rate is $\sim 1.8 \times 10^{-6}$ counts s $^{-1}$ pixel $^{-1}$, although the ETC assumes a more conservative value of $\sim 2.25 \times 10^{-6}$ counts s $^{-1}$ pixel $^{-1}$. The estimated detector background counts for all of the measurements using the on-orbit count rate are listed in Table 2.

Since the detector dark count rate dominates the background signal, we also measure it by a different method as an independent check. Following the procedure outlined in France et al. (2010b), we use the time-tag capability of the COS microchannel plate (MCP) detector to measure the relative contributions of the FUV continuum and background rates, independent of the standard background subtraction applied by the CALCOS pipeline to the one-dimensional science data. For each target, we extract the location-time photon list $[x_i, y_i, t_i]$ from each exposure i and coadd them into a master $[x, y, t]$ list, taking into account the appropriate pixel offsets for exposures made with different central wavelength and FP-POS settings. For the G130M A and B segments, $\Delta\lambda = [1339.8 - 1347.8 \text{ Å}]$ and $[1244.8 - 1253.3 \text{ Å}]$, respectively, we define a detector $[\Delta x, \Delta y]$ location corresponding to the wavelength region of interest ($\Delta\lambda$) and the active science area in the cross-dispersion direction.

We then integrate the total number of counts in the $[\Delta x, \Delta y]$ box in a timestep Δt to compute the count rate in a given spectral window as a function of time. We use a timestep of $\Delta t = 200$ s for this analysis. The instrument background level is computed in a similar manner, with the background integrated over the same $\Delta\lambda$ as the continuum region, but offset below the active science region ($\Delta y_{\text{back}} = \Delta y_{\text{sci}} - 50$ pixels). We show an illustration of the continuum and background count rates (binned by a factor of 2 for display purposes) for HD 209458 in Figure 2. For reference, we also show the count rate of the chromospheric C II 1334+1335 Å emission lines measured with the same method. Because the HD 209458 observing campaign extended over several weeks in 2009 September and October, we plot the count rates as a function of total-integrated observing time as opposed to absolute observing time. We have not included 3,200 s of data when the background was high probably due to the spacecraft being near the South Atlantic Anomaly. One sees that the FUV continuum level is significantly above the instrumental background at almost all times over the 18 individual exposures ($T_{\text{exp}} = 22,441$ s) that went into the master $[x, y, t]$ photon list. Summing over the total exposure time, this method yields an integrated detection significance (σ), defined as the square root of the continuum minus background counts, of $\sigma \sim 42$ for the continuum in

the example shown in Figure 2. Correlation of the continuum and background signals has a Spearman rank correlation index of 0.19 indicating no significant correlation. Applying this technique to all of the stars in our sample, we detect far-UV continua at $\sigma > 12$ in all targets observed by COS. Systematic errors are discussed in the next section.

3. RESULTS

Since the COS spectra have very low detector background noise, we can, for the first time, measure the FUV continuum flux between the emission lines. We have identified several 4–14 Å wide windows with no obvious emission lines in the COS spectra (see Figure 1) and only very weak or no emission lines in the very deep α Cen A (G2 V) spectrum (Pagano et al. 2004). The flux axes in Figure 1 have been set to identify weak emission lines and the flux between the strong emission lines. We convert the average fluxes in these windows (units: $\text{ergs cm}^{-2} \text{s}^{-1} \text{Å}^{-1}$) in Table 2 to stellar surface fluxes using the stellar distances and radii (and their uncertainties) listed in Table 1 and then to equivalent blackbody brightness temperatures (T_B). Figure 3 shows these brightness temperatures in the various windows for the six stars observed with COS, the STIS spectrum of α Cen A, and the Sun (irradiance). For each spectral window, we also list in Table 2 the number of continuum and detector dark counts (using the on-orbit count rate) computed by the ETC. We assume that the measurement errors add in quadrature, that is, the percent measurement errors listed in Table 2 are computed from the square root of the sum of the continuum and dark counts divided by the continuum counts.

There are two other important sources of uncertainty - conversion of observed flux to surface flux and instrument calibration. These uncertainties can be considered systematic as they apply to all data for each star. The ratio of surface to observed flux is proportional to $(d/R)^2$. Table 1 lists the sources of these quantities. Since most of the radii are not accurately measured, we assign generous uncertainties.

As described in the Cycle 19 COS Instrument Handbook Section 6.1.8 and by Massa et al. (2010), the absolute flux calibration of COS is accurate to about 5% in the FUV. Also, time-dependent sensitivity corrections should be accurate to about 2%. The absolute solar fluxes obtained with the SORCE instrument on SOLSTICE II are accurate to about 5% (see above). The absolute flux uncertainty for the STIS E140H spectra depends on wavelength. Bohlin (1998) finds that for the 1325–1510 Å region, the uncertainty is about 4% based on BD+28D4211 as the calibration star, but at shorter wavelengths the uncertainty is 10–20% because BD+75D325 is the calibration star.

Since these four systematic errors (stellar distance, stellar radius, absolute flux calibration, and time-dependent sensitivity correction) are independent, we sum them in quadrature. Finally we sum the systematic and measurement errors in quadrature to obtain the uncertainty in the surface flux and T_B values listed in Table 2.

At wavelengths much shorter than the blackbody emission peak, small changes in T_B correspond to large changes in flux and the brightness temperatures are, therefore, relatively insensitive to the FUV flux errors. For example, at 1415 Å a $\pm 20\%$ error for the solar flux corresponds to $T_B = 4611.6^{+38.5}_{-46.2}$ K, and at 1165 Å the brightness temperature range is $T_B = 5260.2^{+41.1}_{-49.5}$ K. Therefore, the large increases in T_B at all FUV wavelengths for rapidly rotating solar-mass stars compared to the Sun far exceed the flux errors.

4. DISCUSSION

Vernazza et al. (1976) evaluated the then available solar FUV continuum data for disk center (radiance) and flux from the entire Sun (irradiance) using Skylab measurements that were carried out at only a few locations on the solar disk during low solar activity conditions and have uncertain flux-calibration errors. They determined brightness temperatures in the 1300–1700 Å range that cluster about 4500 K for both the disk center radiance and whole disk flux data.

Fontenla et al. (2009) computed a grid of one-dimensional non-LTE model atmospheres to match the observed spectra between the extreme ultraviolet and 100 μm for several types of solar regions defined by their Ca II K line brightness and for sunspot umbrae and penumbrae. Five of the models were computed to match the continuum from the relatively dark quiet-Sun inter-network to bright faculae. Fontenla et al. (2011) improved the transition regions between the chromosphere and corona of these models and included more species whose photoionization and photodissociation opacities replace the *ad hoc* extra FUV opacity used in the Fontenla et al. (2009) models. They also computed two new models, one for very dark (in the Ca II K line) regions of the inter-network and another for the very brightest facular areas seen on the Sun.

The current set of models describes the temperature and density structure as functions of height from the deep photosphere up to the transition region and corona. As with previous solar models by Vernazza et al. (1981) and by Fontenla et al. (1993), the temperature decreases with increasing height in the photosphere reaching a temperature minimum. Above the minimum, the temperature increase in the chromosphere produces the observed FUV continua and lines. The minimum temperature is higher for the brighter models, but un-

like the previous models, the Fontenla et al. (2009 and 2011) models have a temperature minimum that occurs at higher altitudes (corresponding to lower densities) for the darker regions. In the models for the quiet-Sun regions, the temperature minimum value is very low, which explains the CO infrared lines as well as other spectral features that were not explained by the previous models.

In the Fontenla et al. (2011) models, the FUV continuum radiation in the 1300–1500 Å range is produced almost entirely by recombination of Si II, Mg II, and Fe II, and the photospheric radiation is blocked by the photoionization continuum opacity of Si I (with other contributors as well) just below the temperature minimum region. The Si I opacity is largely reduced in the temperature minimum region by the over-ionization (with respect to LTE) caused by UV irradiation from the upper chromosphere; therefore the ionization is much higher than in LTE and is mainly determined by the illumination from the upper chromosphere. Fontenla et al. (2009) noted that the FUV continuum is the most sensitive diagnostic of the slope of the temperature rise in the upper chromosphere.

For each of the models, spectral radiances at 10 points from the solar disk center to the limb are combined to provide the irradiance of a "star" with an atmosphere consisting entirely of this model. We include in Figure 3 brightness temperatures corresponding to the irradiances for each of the Fontenla et al. (2011) models. We plot T_B at four wavelengths (1180.0, 1321.5, 1398.6, and 1500.0 Å) for models 1001 (quiet Sun internetwork), 1002 (quiet Sun network lane), 1003 (enhanced network), 1004 (plage), 1005 (facula), and 1008 (very bright facula). These models correspond to the full range of solar activity and non-radiative heating rates, except for flares. The 2008 April SORCE data, which represents the Sun when it was close to minimum, lies near model 1002 at all four wavelengths. The FUV brightness temperatures for α Cen A, which is a somewhat more evolved and luminous G2 V star than the Sun, lie just below the Sun and generally below solar model 1001.

In Figure 3 the T_B range between the Sun and the most rapidly rotating stars (HII314 and EK Dra) is nearly the same as the range between the quiet Sun inner network and very bright faculae. We note that the stars that rotate about 4 times faster than the Sun (HD 25825, χ^1 Ori, and π^1 UMa) lie well below the fastest rotators (EK Dra and HII314). HD209458, which rotates at twice the speed of the Sun, lies about halfway between the moderately fast rotators and the Sun and α Cen A. Figure 4 compares T_B for the 1382–1392 Å band with the stellar rotation period, P_{rot} . There is a clear trend of increasing T_B with decreasing P_{rot} for the solar-mass stars. The figure shows both linear and quadratic least-squares fits to the data. The second order curve provides a better fit to the data.

The increase in T_B to shorter wavelengths for the rapidly-rotating solar-mass stars is similar to that of the slowly-rotating Sun and the models for regions of different activity on

the Sun. This is expected as the models for regions on the Sun with increasing activity have temperature structures with height that are similar in shape near and above the temperature minimum. Increasing temperature and thus ionization lead to higher FUV continuum emission, unless the opacity sources change dramatically. The agreement of the FUV continuum fluxes of the rapidly-rotating solar-mass stars with the models for the brightest regions on the Sun indicate that the models for active regions on the Sun provide first order approximations to the temperature minimum and chromospheric thermal structure of the rapidly-rotating stars.

The one-dimensional Fontenla et al. (2011) models also predict fluxes of emission lines formed above the photosphere, but the thermal structure of the Solar chromosphere and higher layers is far more complex than even a mixture of one-component models due to absorption by overlying filament structures, time-dependent heating, and dynamics. Active stars presumably also have such properties. The fluxes and profiles of optically thick emission lines formed in the chromosphere will likely be most affected by three-dimensional structures. Optically thick resonance line profiles of O I and C II, therefore, may not be well fit by one-dimensional Solar models. A better test of our comparison of active stars to active regions on the Sun should be the lower opacity Si IV 1393 Å emission line formed in the transition region between the chromosphere and corona. Figure 5 compares the stellar line fluxes with those of the Fontenla et al. (2011) models. The stellar Si IV fluxes are plotted against the 1382–1392 Å stellar continuum flux, both at a distance of 1 AU. For comparison, Si IV fluxes are plotted against the 1398.6 Å continuum fluxes for the models, also assuming a distance of 1 AU. Except for HD 209458, the model predictions are close to the observations. The observations and models both show the same trend of increasing line and continuum flux with increasing stellar rotation and Solar activity.

5. CONCLUSIONS

We show that the high throughput and low detector noise of the COS permits the detection of FUV continuum emission from solar-mass stars for the first time. The observed FUV brightness temperatures obtained from the solar irradiance and from the somewhat more evolved G2 V star α Cen A are very similar between 1150 and 1500 Å, indicating that the absolute flux scales of HST and SORCE are compatible. We find a clear trend of increasing FUV continuum brightness temperatures with more rapid rotation for the six solar-mass stars observed by COS, α Cen A, and the Sun. Comparison with semiempirical models for different regions on the Sun shows that the FUV continuum brightness temperatures derived from the surface fluxes of the most rapidly rotating stars in our sample are

similar to or slightly exceed those of the brightest facular regions on the Sun. Since the FUV continuum flux is the most sensitive diagnostic of the thermal structure of the lower Solar chromosphere, we believe that the now measurable FUV continuum fluxes of solar-mass stars and likely a much wider range of stars with convective zones will be very useful sensitive diagnostics of the thermal structures of their chromospheres. The broad range of possible applications of this new chromospheric diagnostic should be explored in future papers. In particular, the FUV continuum diagnostic should provide new information on the amount of magnetic heating in the chromospheres of rapidly rotating and thus active stars. This is important both for our understanding of stellar physical processes and because FUV photons strongly affect the atmospheric chemistry and heating of exoplanets through the excitation and dissociation of such molecules as H_2O , CH_4 , and CO_2 .

This work is supported by NASA through grants NNX08AC146, NAS5-98043, and HST-GO-11687.01-A to the University of Colorado at Boulder. We thank Tom Woods for providing the SORCE data and Steven Osterman for information on the COS calibration.

Facilities: HST (COS), HST (STIS). SIMBAD

REFERENCES

- An, D., Terndrup, D. M., Pinsonneault, M. H., Paulson, D. B., Hanson, R. B., & Stauffer, J. R. 2007, *ApJ*, 655, 233
- Avrett, E. H. and Loeser, R. 2008, *ApJS*, 175, 229
- Ayres, T. R. 2010, *ApJS*, 187, 149
- Ayres, T., & France, K. 2010, *ApJ*, 723, L38
- Ayres, T. R. 1999, *ApJ*, 525, 240
- Barnes, S. A. 2007, *ApJ*, 669, 1167
- Bohlin, R. 1998, STIS Instrument Science Report 98-18, Space Telescope Science Institute (Baltimore, MD)
- de Meulenaer, P., Carrier, F., Miglio, A., Bedding, T. R., Campante, T. L., Eggenberger, P., Kjeldsen, H., & Montalbán, J. 2010, *A&A*, 523, A54
- Fontenla, J. M., Avrett, E. H., & Loeser, R. 1993, *ApJ*, 406, 319

- Fontenla, J. M., Curdt, W., Haberreiter, M., Harder, J., & Tian, H. 2009, *ApJ*, 707, 482
- Fontenla, J. M., Harder, J., Livingston, W., Snow, M., & Woods, T. 2011, *JGR-Atmospheres*, in press, doi:10-1029/2001J016032
- Franchini, M., Morossi, C., & Malagnini, M. L. 1998, *ApJ*, 508, 370
- France, K., Stocke, J. T., Yang, H., Linsky, J. L., Wolven, B. C., Froning, C. S., Green, J. C., & Osterman, S. N. 2010a, *ApJ*, 712, 1277
- France, K., Linsky, J. L., Brown, A., Froning, C. S., & Béland, S. 2010b, *ApJ*, 715, 596
- Gaidos, E. J., Henry, G. W., & Henry, S. M. 2000, *AJ*, 120, 1006
- Järvinen, S. P., Berdyugina, S. V., Korhonen, H., Ilyin, I., & Tuominen, I. 2007, *A&A*, 472, 887
- King, J. R., & Schuler, S. C. 2005, *PASP*, 117, 911
- Knutson, H. A., Charbonneau, D., Noyes, R. W., Brown, T. M., & Gilliland, R. L. 2007, *ApJ*, 655, 564
- Kraft, R. P. 1967, *ApJ*, 150, 551
- Linsky, J. L., Yang, H., France, K., Froning, C. S., Green, J.C., Stocke, J. T., & Osterman, S. N. 2010, *ApJ*, 717, 1291
- Massa, D., Keyes, C., Penton, S., Bohlin, R., & Froning, C. 2010, *SMOV Absolute Flux Calibration of the COS FUV Modes*, Instrument Science Report COS 2010-02(v1), Space Telescope Science Institute (Baltimore, MD)
- Matt, S. & Pudritz, R.E. 2008, *ApJ*, 681, 391
- McClintock, W. E., Snow, M., & Woods, T. N. 2005, *Sol. Phys.*, 230, 259
- Morossi, C., Franchini, M., Malagnini, M. L., Kurucz, R. L., & Buser, R. 1993, *A&A*, 277, 173
- Morossi, C., Franchini, M., Malagnini, M. L., & Chavez, M. A. 2003, *Proceedings of the 12th Cambridge Workshop on Cool Stars, Stellar Systems, and the Sun: Univ. Colorado: Boulder*), p. 285
- Nordström, B. et al. 2004, *A&A*, 418, 989

- Osterman, S. N. et al. 2002, Proc. SPIE no. 4485, 361
(http://cos.colorado.edu/COS_publications/SO_8.2.01.pdf)
- Osterman, S. N., et al. 2011, Ap&SS, in press (arXiv:1012.5827)
- Pagano, I., Linsky, J. L., Valenti, J., & Duncan, D. K. 2004, A&A, 415, 331
- Pizzolato, N., Maggio, A., Micela, G., Sciortino, S., & Ventura, P. 2003, A&A, 397, 147
- Radick, R. R., Thompson, D. T., Lockwood, G. W., Duncan, D. K., Baggett, W. E. 1987, ApJ, 321, 459
- Ribas, I., Guinan, E. F., Güdel, M., & Audard, M. 2005, ApJ, 622, 680
- Rice, J. B., & Strassmeier, K. G. 2001, A&A, 377, 264
- Silva-Valio, A. 2008, ApJ, 683, L179
- Simon, T., Herbig, G., & Boesgaard, A. M. 1985, ApJ, 293, 551
- Snow, M., McClintock, W. E., Rottman, G., & Woods, T. N. 2005, Sol. Phys., 230, 295
- Strassmeier, K. G., & Rice, J. B. 1998, A&A, 330, 685
- Vernazza, J. E., Avrett, E. H., & Loesser, R. 1976, ApJS, 30, 1
- Vernazza, J. E., Avrett, E. H., & Loesser, R. 1981, ApJS, 45, 635
- Vieytes, M., Mauas, P., & Cincunegui, C. 1995, A&A, 441, 701
- Wilson, O. C. 1963, ApJ, 138, 832
- Woods, T. N., et al. 2009, J. Geophys. Res., 36, L01101

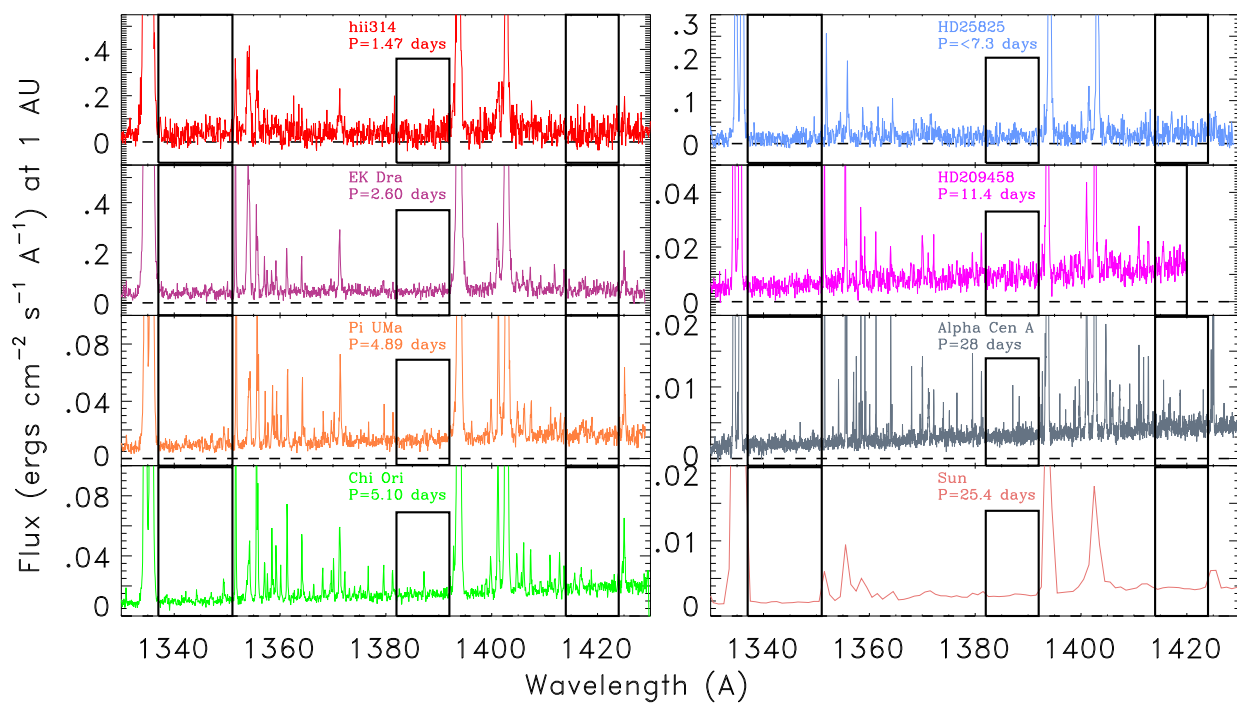


Fig. 1.— Comparison of the spectra of the six solar-mass stars observed with COS, the STIS spectrum of α Cen A, and the SORCE solar flux spectrum. The flux axes are set to identify weak emission lines and the stellar continua. The centers of bright emission lines of C II (1334 and 1335 Å) and Si IV (1394 and 1403 Å) are off scale. The windows used for continuum measurements are indicated.

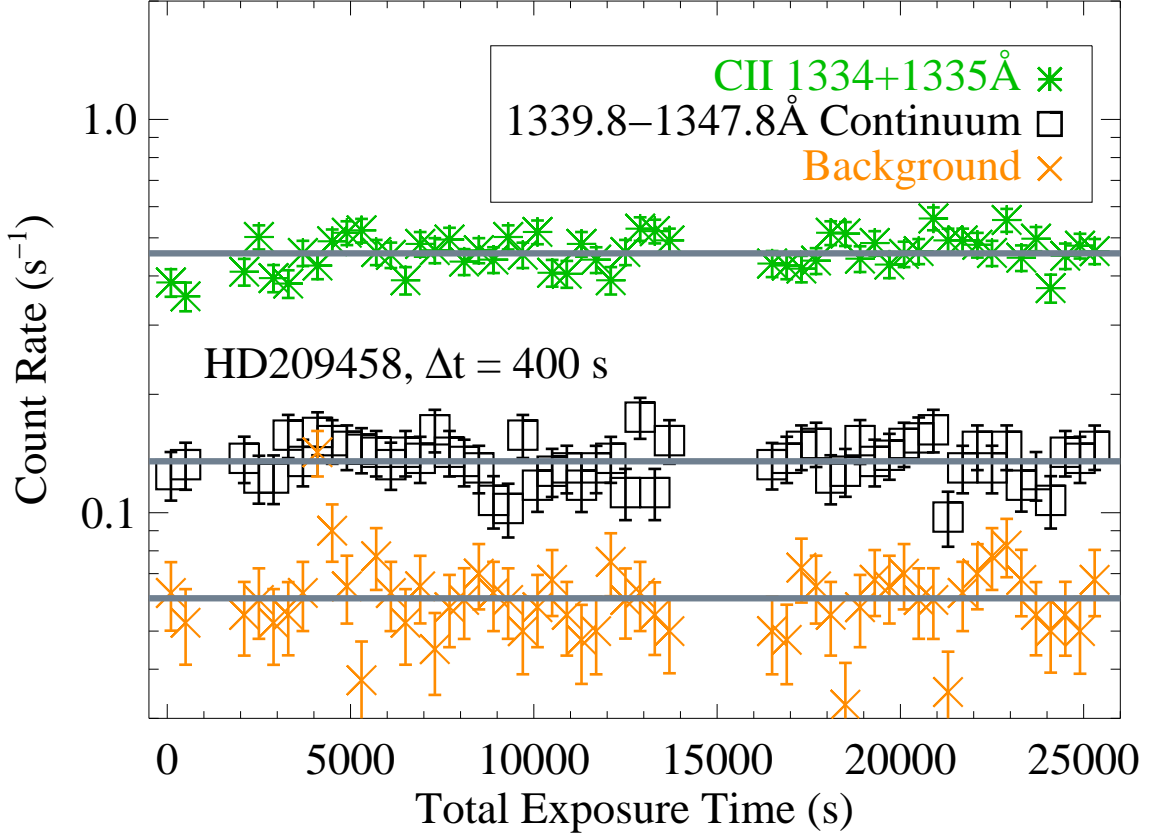


Fig. 2.— The count rate of the G130M segment A continuum ($1339.8 \lesssim \lambda \lesssim 1347.8$) in HD 209458 (shown as black squares) is compared with the detector background level measured immediately below the active science area (shown as orange x’s). The coadded $[x,y,t]$ photon list was sampled at 200 s intervals, and the data have been rebinned by a factor of two for display purposes. As the HD 209458 observing program spanned ~ 6 weeks, we show the count rates as a function of the total observing time. We have removed data in two time intervals of high background (800–1800 and 14000–16200 s) probably during spacecraft passage near the South Atlantic Anomaly. The gray solid lines represent the average count rates. For reference, the count rate of the bright chromospheric emission lines from C II 1334, 1335 Å are shown as the green stars.

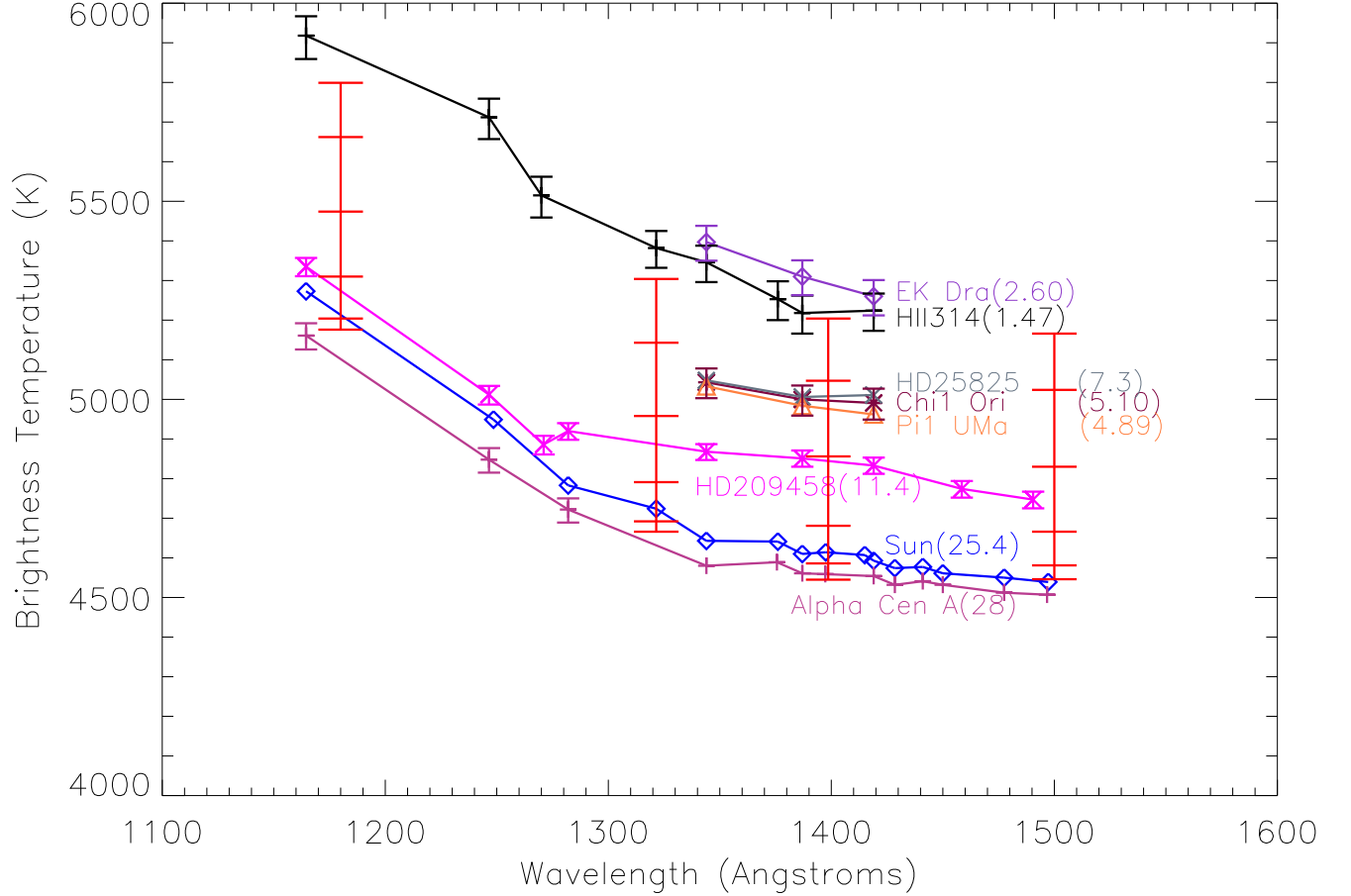


Fig. 3.— Brightness temperatures vs. wavelength for the six solar-mass stars observed with COS, α Cen A observed with STIS, and the solar flux measured by the SORCE instrument at a time of very low activity. The rotational periods of the stars and the sidereal period of the Sun are in parentheses. Error bars computed from the measurement and systematic errors listed in Table 2 are shown when the errors are greater than the symbol sizes. The error bars for χ^1 Ori are also representative for HD25825 and π^1 UMa. The horizontal bars centered at wavelengths 1180, 1321.5, 1398.6, and 1500.0 Å indicate the predicted brightness temperatures for 6 solar irradiance models computed by Fontenla et al. (2009) and Fontenla et al. (2011) for the Quiet Sun inner network (lowest bar) up to a very bright facula (Models 1001 to 1005 and 1008).

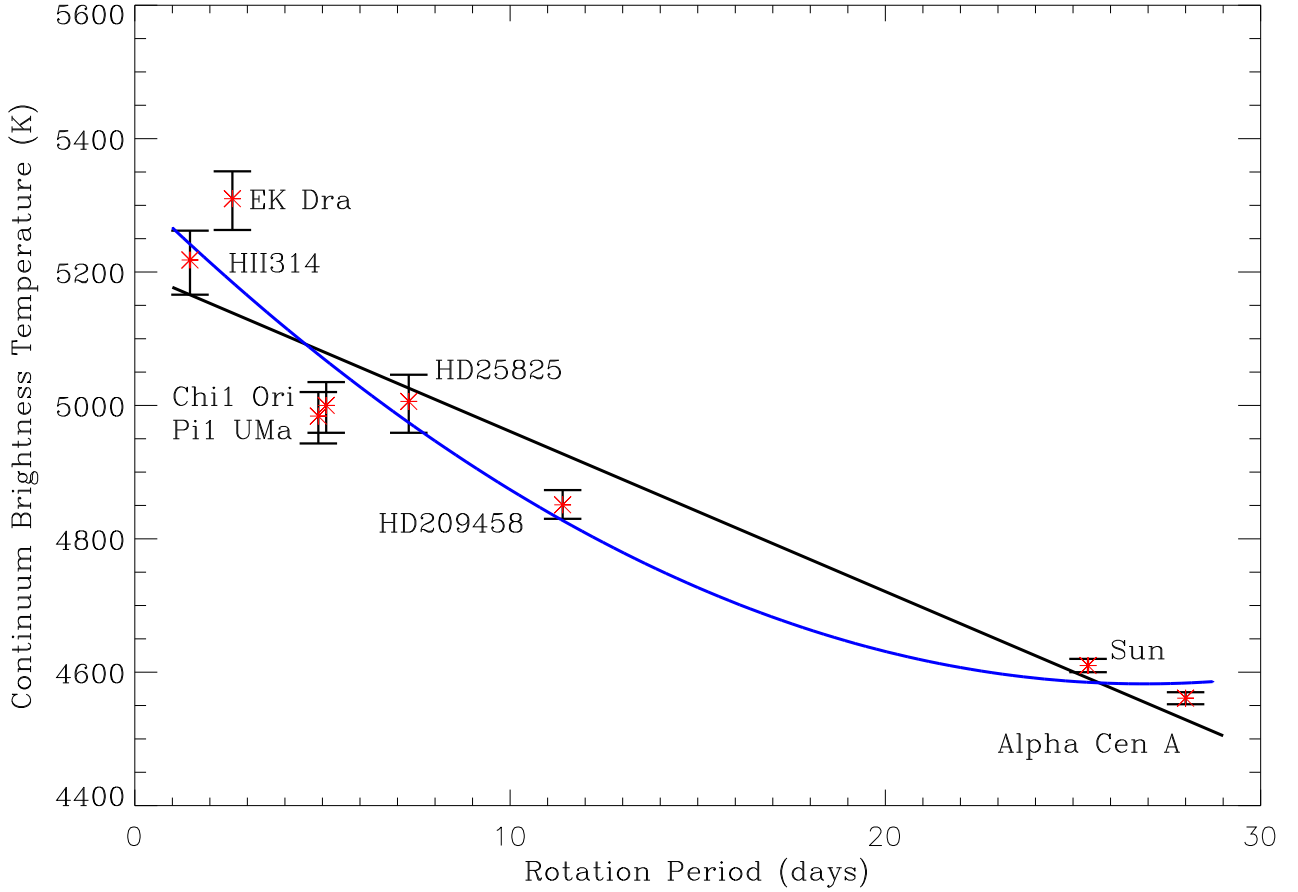


Fig. 4.— Comparison of the 1382-1392 Å continuum brightness temperatures with rotation periods for the identified stars. The black line is a least-squares linear fit to the data, $T_B = 5201.14 - 24.0148P_{\text{rot}}$. The blue line is a least-squares quadratic fit to the data, $T_B = 5320.17 - 54.8303P_{\text{rot}} + 1.01890P_{\text{rot}}^2$.

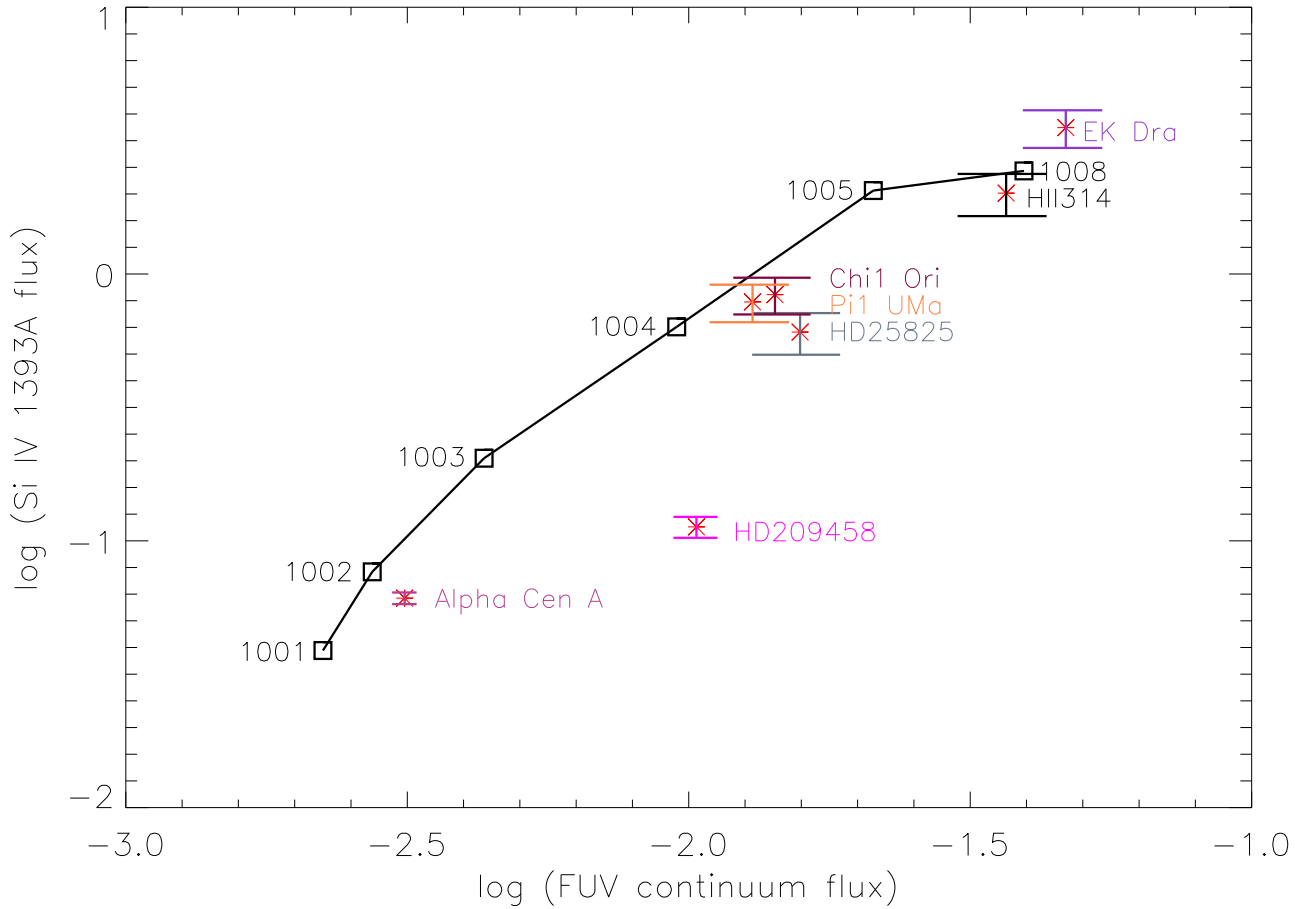


Fig. 5.— Asterisk symbols are for the observed Si IV 1393 Å stellar fluxes plotted vs stellar 1382–1392 Å continuum fluxes both at a distance of 1 AU. The individual stars are identified. The square symbols plot the predicted Si IV 1393 Å flux vs 1398.6 Å continuum flux of the Fontenla et al. (2011) models also at a distance of 1 AU. The models numbers are marked.

Table 1. Stellar Properties and Observing Log

Star	$P_{\text{rot}}(\text{days})^{\text{a}}$	Age(10^9 yr)	d(pc) ^b	R/R_{\odot}^{c}	Instrument	Dataset	Grating	Central λ	$T_{\text{exp}}(\text{s})$
HII314	1.47	0.1	135.8 ± 3.0	1.0 ± 0.10	COS	LB6401010	G130M	1309	814.1
HII314	1.47	0.1	135.8 ± 3.0	1.0 ± 0.10	COS	LB6401020	G130M	1318	990.1
HII314	1.47	0.1	135.8 ± 3.0	1.0 ± 0.10	COS	LB6401030	G130M	1291	1402.0
HII314	1.47	0.1	135.8 ± 3.0	1.0 ± 0.10	COS	LB6401040	G130M	1300	1405.2
EK Dra	2.60	0.03–0.05	34.1 ± 0.4	0.95 ± 0.10	COS	LB3E34010	G130M	1291	1160.0
π^1 UMa	4.89	0.3	14.36 ± 0.08	0.95 ± 0.10	COS	LB3E26010	G130M	1291	1300.4
χ^1 Ori	5.10	0.3	8.66 ± 0.02	0.96 ± 0.10	COS	LB3E06010	G130M	1291	1300.4
HD25825	7.3	0.6	45.9 ± 2.7	1.0 ± 0.10	COS	LB3E41010	G130M	1291	1160.0
HD209458	11.4	4 ± 2	49.6 ± 2.0	1.125 ± 0.023	COS	LB4M ^b	G130M		22441.0
α Cen A	28	3.9–4.9	1.325 ± 0.007	1.224 ± 0.003	STIS		E140H	1234	4695.2
α Cen A	28	3.9–4.9	1.325 ± 0.007	1.224 ± 0.003	STIS		E140H	1416	4695.2
Solar flux	25.4	4.6			SORCE				

^aRotation Periods: HII314 (Rice & Strassmeier 2001), EK Dra (Strassmeier & Rice 1998; Järvinen et al. 2007), π^1 UMa (Gaidos et al. 2000), χ^1 Ori (King & Schuler 2005), HD25825 (mean of 4 Hyades stars with B–V = 0.59–0.61 (Radick et al. 1987)), HD209458 (Silva-Valio 2008), α Cen A (Barnes 2007).

^bData from SIMBAD except for HII314 for which we have used the An et al. (2007) distance to the Pleiades.

^cData from Ribas et al. (2005) except for HD 209458 (Knutson et al. 2007), α Cen A (de Meulenaer et al. 2010), and HII314 (Ayres 1999). Errors for the other stars are generous estimates.

Table 2. Far-UV Continuum Fluxes and Brightness Temperatures

Star	Wavelength Range	Flux (cgs)	Surface Flux ^a	Continuum Counts	Dark Counts	Ratio (C/D)	Measurement Error(%)	Systematic Error(%)	T _B (K)
HII314	1158–1171	4.13E-17	1497 ± 282	257	508	0.51	10.8	15.4	5918 ⁺⁴⁹ ₋₅₉
	1244–1249	5.76E-17	2085 ± 374	223	195	1.14	9.2	15.4	5712 ⁺⁴⁷ ₋₅₅
	1267–1273	3.75E-17	1358 ± 259	182	234	0.78	11.2	15.4	5515 ⁺⁴⁷ ₋₅₆
	1315–1328	4.20E-17	1520 ± 265	358	508	0.70	8.2	15.4	5382 ⁺⁴³ ₋₅₀
	1337–1351	4.73E-17	1713 ± 293	418	547	0.76	7.4	15.4	5346 ⁺⁴² ₋₅₀
	1372–1380	4.74E-17	1717 ± 317	229	312	0.73	10.2	15.4	5253 ⁺⁴⁵ ₋₅₃
	1382–1392	4.67E-17	1692 ± 305	273	391	0.70	9.4	15.4	5218 ⁺⁴⁴ ₋₅₂
	1414–1424	6.69E-17	2424 ± 420	343	391	0.88	7.9	15.4	5224 ⁺⁴³ ₋₅₁
EK Dra	1337–1351	8.18E-16	2071 ± 333	1826	138	13.2	2.4	15.9	5397 ⁺⁴¹ ₋₄₇
	1382–1392	9.45E-16	2393 ± 386	1396	99	14.1	2.8	15.9	5310 ⁺⁴¹ ₋₄₇
	1414–1424	1.09E-15	2760 ± 446	1406	99	14.2	2.8	15.9	5260 ⁺⁴¹ ₋₄₈
π ¹ UMa	1337–1351	1.10E-15	494 ± 79.2	2752	155	17.8	2.0	15.9	5033 ⁺³⁵ ₋₄₁
	1382–1392	1.48E-15	665 ± 107	2452	111	22.1	2.1	15.9	4984 ⁺³⁶ ₋₄₁
	1414–1424	1.93E-15	867 ± 139	2792	111	25.2	1.9	15.9	4962 ⁺³⁶ ₋₄₂
χ ¹ Ori	1337–1351	3.22E-15	515 ± 81.1	8054	155	52.0	1.1	15.7	5043 ⁺³⁵ ₋₄₀
	1382–1392	4.46E-15	713 ± 112	7390	111	66.6	1.2	15.7	5000 ⁺³⁵ ₋₄₁
	1414–1424	6.12E-15	979 ± 154	8854	111	79.8	1.1	15.7	4991 ⁺³⁶ ₋₄₂
HD25825	1337–1351	1.27E-16	526 ± 93.9	283	138	2.04	7.3	16.3	5048 ⁺³⁹ ₋₄₆
	1382–1392	1.76E-16	729 ± 130	261	99	2.63	7.3	16.3	5006 ⁺⁴⁰ ₋₄₇
	1414–1424	2.56E-16	1060 ± 185	331	99	3.34	6.3	16.3	5011 ⁺⁴⁰ ₋₄₇
HD209458	1158–1171	4.00E-17	153 ± 15.3	1216	2469	0.49	5.0	8.66	5335 ⁺²² ₋₂₄
	1244–1249	3.24E-17	124 ± 13.4	611	949	0.64	6.5	8.66	5012 ⁺²² ₋₂₅
	1268–1274	2.56E-17	97.6 ± 10.8	606	1139	0.53	6.9	8.66	4886 ⁺²² ₋₂₅
	1277–1287	3.52E-17	134 ± 12.9	1374	1899	0.72	4.2	8.66	4920 ⁺²² ₋₂₂
	1337–1351	6.28E-17	240 ± 21.8	2704	2658	1.02	2.7	8.66	4868 ⁺¹⁹ ₋₂₁
	1382–1392	9.86E-17	376 ± 33.8	2814	1899	1.48	2.4	8.66	4851 ⁺²⁰ ₋₂₁
	1414–1424	1.32E-16	504 ± 45.0	3289	1899	1.73	2.2	8.66	4833 ⁺²⁰ ₋₂₁
	1456–1461	1.58E-16	602 ± 53.9	2520	949	2.66	2.3	8.66	4774 ⁺²⁰ ₋₂₂
	1487–1494	1.96E-16	750 ± 66.5	3674	1329	2.76	1.9	8.66	4747 ⁺²⁰ ₋₂₂
	α Cen A ^b	1158–1171	3.05E-14	70.2 ± 11.5	2023	12548	0.16	6.0	15.2
1244–1249		2.47E-14	56.9 ± 8.75	4085	4511	0.91	2.3	15.2	4848 ⁺²⁹ ₋₃₃
1277–1287		2.24E-14	51.6 ± 7.88	8766	8766	1.00	1.5	15.2	4722 ⁺²⁸ ₋₃₃
1337–1351		2.62E-14	60.3 ± 2.70	14986	11708	1.28	1.1	4.34	4580 ± 09
1372–1379.3		4.17E-14	96.0 ± 4.30	12044	5923	2.03	1.1	4.34	4589 ± 09
1382–1392		4.19E-14	96.5 ± 4.30	14506	8104	1.79	1.0	4.34	4561 ± 09
1396.1–1398.6		4.68E-14	109 ± 5.21	3921	2011	1.95	2.0	4.34	4559 ± 09
1414–1424		6.03E-14	139 ± 6.13	20294	7921	2.56	0.8	4.34	4554 ± 09
1426–1431		6.10E-14	140 ± 6.30	9991	3934	2.54	1.2	4.34	4532 ± 09
1438–1444		7.40E-14	170 ± 7.57	13542	4680	2.89	1.0	4.34	4541 ± 09
Sun ^c	1446–1454	7.88E-14	181 ± 8.02	16266	6201	2.62	0.9	4.34	4532 ± 09
	1475–1480	9.75E-14	225 ± 10.0	11987	3422	3.50	1.0	4.34	4512 ± 09
	1494.5–1500	1.19E-13	274 ± 12.1	14746	4129	3.57	0.9	4.34	4507 ± 09
	1158–1171	2.53E-03	117 ± 5.4					5.0	5273 ± 10
	1244–1253	2.06E-03	95.2 ± 4.8					5.0	4949 ± 11
	1277–1287	1.51E-03	69.8 ± 3.6					5.0	4783 ± 10

Table 2—Continued

Star	Wavelength Range	Flux (cgs)	Surface Flux ^a	Continuum Counts	Dark Counts	Ratio (C/D)	Measurement Error(%)	Systematic Error(%)	T _B (K)
	1315–1328	1.97E-03	90.9 ± 4.6					5.0	4724 ± 10
	1337–1351	1.79E-03	82.9 ± 4.3					5.0	4643 ± 10
	1371–1381	2.70E-03	125 ± 6.4					5.0	4641 ± 10
	1382–1392	2.67E-03	123 ± 6.3					5.0	4610 ± 10
	1396–1399	3.10E-03	143 ± 7.4					5.0	4614 ± 10
	1408–1422	3.70E-03	171 ± 8.7					5.0	4607 ± 10
	1414–1424	3.64E-03	168 ± 8.5					5.0	4593 ± 10
	1426–1431	3.72E-03	172 ± 8.8					5.0	4574 ± 11
	1438–1444	4.37E-03	202 ± 10.3					5.0	4577 ± 11
	1446–1454	4.51E-03	208 ± 10.6					5.0	4561 ± 11
	1475–1480	5.83E-03	270 ± 13.4					5.0	4550 ± 11
	1494.5–1500	6.89E-03	318 ± 16.3					5.0	4539 ± 11

^aSurface fluxes (units: $\text{ergs cm}^{-2} \text{ s}^{-1} \text{ \AA}^{-1}$) computed using the stellar distances and radii listed in Table 1. Flux errors are computed from a quadratic sum of the measurement and systematic errors.

^bObserved with the STIS E140H grating.

^cObserved by SORCE.